NATIONAL AERONAUTICS AND SPACE ADMINISTRATION

Technical Memorandum 33-610

Mariner Mars 1971 Sun Sensor Model Development and Simulation

L. Schumacher

JET PROPULSION LABORATORY

CALIFORNIA INSTITUTE OF TECHNOLOGY

PASADENA, CALIFORNIA

May 1, 1973

NATIONAL AERONAUTICS AND SPACE ADMINISTRATION

Technical Memorandum 33-610

Mariner Mars 1971 Sun Sensor Model Development and Simulation

L. Schumacher

JET PROPULSION LABORATORY
CALIFORNIA INSTITUTE OF TECHNOLOGY
PASADENA, CALIFORNIA

May 1, 1973

PREFACE

The work described in this report was performed by the Guidance and Control Division of the Jet Propulsion Laboratory.

Page Intentionally Left Blank

CONTENTS

I. Introduction 1

II. The Cadmium Sulfide Photodetector 2

A. The Photodetector Container 3

B. The Operating Characteristics of the Mariner 1971 Cadmium Sulfide Photodetector 3

III. The Mariner 1971 Cruise Sun Sensor 7

A. Physical Description 7

B. The Theory and Operation of the Mariner 1971 Cruise Sun Sensor 8

C. The Mariner 1971 Cruise Sun Sensor Model 10

IV. The Mariner 1971 Acquisition Sun Sensors 14

A. Physical Configuration 14

B. Acquisition Sun Sensor Performance Model 14

V. The Mariner 1971 Pitch and Yaw Axis Control Electronics 16

A. Introductory Remarks 16

B. Attitude Control Electronics Model 17

VI. The Mariner 1971 Sun Sensor Life Test and Simulation Results 20

A. Introductory Remarks 20

B. The Cruise Sun Sensor Aging Test (No Rotation) 21

C. The Cruise Sun Sensor Aging Test (With Rotation) 22

D. Mariner 9 Flight Simulation 24

E. Mariner 1971 Acquisition Sun Sensor Simulations 26

VII. Conclusion and Recommendations 27

References 29

Appendix. Determination of the Illumination Profile Over the Cruise Sun Sensor Detector Width 43

CONTENTS (contd)

FIGURES

1. Cadmium sulfide detector configuration 30
2. Fully illuminated CdS detector resistance as a function of illumination 30
3. Detector coordinate system 31
4. Mariner 71 cruise Sun sensor configuration 31
5. Mariner 71 cruise sensor field-of-view 32
6. Sun side (top) view of Mariner 71 spacecraft 32
7. Theory of cruise sensor operation 33
8. Idealized detector pair aging with unequal rate of aging 33
9. Cruise Sun sensor illumination profile over detector width 34
10. Acquisition Sun sensor 34
11. Acquisition Sun sensor pair showing field stops and shadow bar configuration 35
12. Mariner 71 pitch axis acquisition Sun sensor field-of-view 35
13. Mariner 71 yaw axis acquisition Sun sensor field-of-view 36
14. Acquisition detector resistance vs conical error angle of a 64,560-lm/m^2 (6,000-ft-cd) light source 36
15. Forward-looking acquisition detector resistance vs cone angle of a 64,560-lm/m^2 (6,000-ft-cd) light source 37
16. Mariner 71 pitch and yaw axes Sun sensor control circuit 37
17. Evaluation of limit cycle rate increment due to a gas pulse 37
18. Estimates of Mariner 9 deadband halfwidth 38
19. Analytic pitch and yaw axis control circuit 38

FIGURES (contd)

20. Mariner 71 cruise detector resistance during a life test without detector rotation 38

21. Mariner 71 cruise detector resistance during a life test with detector rotation 39

22. Aging gain as a function of fixed light intensity and time 39

23. Comparison of flight-observed half-deadband width to the computer model half-deadband width 40

24. Cruise sensor sensitivity 40

25. Resistance values of simulated cruise Sun sensor elements 41

26. Voltage drop across Sun sensor bridge 41

27. Sun sensor resistances near periapsis, December 10, 1971 42

28. The illuminated portion of Mars as observed on the spacecraft 42

A-1. Relation of solar disk coordinates to spacecraft detector coordinates 44

ABSTRACT

The Mariner 9 spacecraft was launched with an incorrectly sized resistor at the Sun sensor circuit interface with its power supply. The design error caused 72 days of anomalous spacecraft operation, and it became apparent that some facets of Sun sensor performance and the cadmium sulfide aging phenomena were not well understood. The object of this study was to analyze the Sun sensor flight performance data and the results of a newly developed cruise sensor life test in order to better understand cadmium sulfide Sun sensor performance.

A set of mathematical models was constructed which closely approximated the observed Sun sensor flight and laboratory test results. These models revealed, among other things, that (1) the aging phenomena in the sintered cadmium sulfide light detector varies across the detector width in proportion to the illumination history, (2) the current cruise Sun sensor design is extremely sensitive to changes in the reflected illumination within the sensor housing, (3) the reflected illumination within the detector housing is proportional to the area and intensity of the solar disk observed at the spacecraft, and (4) the acquisition Sun sensor becomes a low impedance path across the sensor bridge when in the vicinity of a large-angular-diameter, low-intensity light source.

It is concluded that a computer model can be developed which will accurately predict Sun sensor performance in a variety of flight conditions.

For future missions it is proposed that a Sun sensor analysis and model development program be instituted in support of a comprehensive test program so that the performance of future Sun sensor designs may be more fully evaluated prior to flight.

I. INTRODUCTION

After the launch of Mariner 71, the flight telemetry data revealed that the spacecraft pitch and yaw Sun sensor circuits were not performing in the anticipated manner. It was discovered that a resistor at the interface between the Sun sensor bridge circuit and its power supply had been sized incorrectly. The anomalous flight performance due to the design error was offset somewhat by the opportunity to observe the cruise detector aging phenomena. However, predictions of cruise detector aging based on preflight laboratory tests did not agree with the observed flight data.

Subsequent to launch, a new life test procedure was developed which did reproduce many of the observed Sun sensor flight characteristics but did not explain the mechanism of these observed phenomena.

The object of this report is to investigate the Mariner 71 Sun sensor performance and attempt to provide some insight into the Sun sensor operation and aging phenomena. The investigation utilized a set of computer models which closely approximated the observed flight and test data.

The model set consists of object models and environmental models. The object models include the following:

(1) A single light detector model that includes aging effects.

(2) A cruise Sun sensor model that specifies the illumination distribution on the detector surface as a function of the angular diameter and offset of the light source.

(3) An acquisition sensor model that determines the resistance of each acquisition detector given the clock and cone angles and the illuminance produced by the light source.

(4) An attitude control electronics model that is a detailed model of the pitch and yaw control circuitry, which determines the position deadband values.

The environmental models attempt to reproduce the space environment during flight and the cruise sensor life tests.

These models include the following:

(1) The illumination and angular diameter of the light source as a function of the radial distance from the Sun.

(2) The reflected illumination within the cruise sensor housing.

A detailed description of each model and comments on the development of these models follows.

II. THE CADMIUM SULFIDE PHOTODETECTOR

The photodetector consists of two parts, a light-sensitive material deposited on a ceramic wafer and a housing for this wafer.

Sintered cadmium sulfide was used as the Mariner 71 Sun sensor photodetector material. The detectors are manufactured by floating a slurry of cadmium sulfide on the surface of a pool of water and raising a ceramic wafer through the surface slurry. The film thickness and uniformity of the CdS layer on the ceramic wafer are determined by the slurry characteristics and the amount used. Each wafer is baked in an oven and the result is a thick, hard, CdS crystalline deposit on the ceramic base. Since a photodetector measures the surface response of the light-sensitive material, the desired light-sensitive region is left exposed and the rest of the CdS surface is masked with an opaque material. The exposed light-sensitive area on the Mariner 71 detectors measures 0.127 by 0.594 cm (0.05 by 0.234 in.).

The cadmium sulfide acts as a light-sensitive resistor. The resistance is measured across the narrow dimension of the exposed light-sensitive area. Indium electrodes are deposited on the long edges of the light-sensitive detector area, and lead wires are soldered to these electrodes as illustrated in Fig. 1.

A. The Photodetector Container

The ceramic wafer with a precisely masked photosensitive region is housed in a TO-5 size transistor can with a window to admit solar radiation. This container is well suited for Sun sensor use, providing the detector with protection from physical damage and an efficient heat dissipation medium. Figure 1 shows a cutaway view of the detector and the TO-5 container. Note that movement of the ceramic wafer is prevented by the electrical leads, which are crimped over to hold the wafer against the header assembly.

Vibration tests have fractured the indium solder joints, but a silicone rubber coat on the rear of the TO-5 cans and Teflon bushing have succeeded in isolating the vibration-induced stresses so that no failures have been observed in tests using the new resilient mount.

B. The Operating Characteristics of the Mariner 1971 Cadmium Sulfide Photodetector

The surface of the exposed sintered cadmium sulfide acts as a light-sensitive resistor. The resistance characteristics are a function of the detector material, the exposed area, and the illumination. The detector material properties vary over the surface of each detector and from batch to batch in the manufacturing processes. The resistance of sintered cadmium sulfide versus illumination was estimated from manufacturers' data, Ref. 1, and unpublished test data taken at JPL. The approximate resistance of a fully and uniformly illuminated unaged detector as a function of light intensity is illustrated in Fig. 2, and the mathematical expression for this resistance is given as follows:

$$RU(E) = \exp\left[13.595 - 0.6021 \log(E)\right] \tag{1}$$

where

$RU(E)$ = the resistance of a fully illuminated unaged detector

E = the illumination level in lm/m^2 at the detector surface.

It will be assumed in the analysis that follows that all cadmium sulfide detectors used in both the cruise and acquisition sensors have the fully illuminated, unaged, resistance characteristic described in Eq. (1).

All the cruise sensors and four of the acquisition sensors are at least partially shadowed during normal cruise operation. To accurately determine the resistance of each detector, an expression for the resistance of a partially illuminated detector is required. The following rationale was used in developing the expression for the resistance of a nonuniformly illuminated detector.

(1) When the Sun is within 2 deg of the cruise sensor null axis, the illumination may vary over the width of the detector but is uniform over the detector length, as illustrated in Fig. 3.

(2) An infinitesimal width of a detector (dz in Fig. 3) will have a resistance proportional to its width relative to the resistance of a fully illuminated detector illuminated at the same intensity. The partial detector resistance may be expressed as follows.

$$dR = \frac{RU(E)\, dz}{w} \tag{2}$$

where

dR = the resistance of a detector segment of length ℓ, width dz, and illumination E, when measured across width dz.

RU(E) = the resistance of a fully illuminated detector of length ℓ, width w, and constant uniform illumination E, when measured across the width w. This data is obtained from manufacturer and test data.

In general, the illumination will vary across the detector width and can be expressed as E(z), where z is a linear measure of the relative detector position from the center of the detector. The illumination profile E(z) over the detector width is a function of the cruise Sun sensor design. Details of the Mariner 71 cruise Sun sensor design and evaluation of the illumination profile as a function of the position on the detector width will be given in the next section.

(3) The resistance of a nonuniformly illuminated detector is the sum of the partial resistances of the segments of that detector. This resistance is expressed as follows.

$$R[E(z)] = \int_{-w/2}^{w/2} dR$$

$$= \int_{-w/2}^{w/2} \frac{RU[E(z)]}{w}\, dz \qquad (3)$$

In addition to the effects of nonuniform illumination, each segment dz of the detector width may change its resistance as the duration and magnitude of exposure to solar radiation changes. This effect is called aging; its precise nature is not known. Reference 2 indicates that desorption of O_2 molecules in the photoconductive layers is the probable cause of the change in electrical properties. Even though the precise nature of this phenomenon is not known, a mathematical model was developed which closely approximates the aging response at uniform temperatures.

Absorption-desorption processes are very often approximately exponential in nature. Therefore, an exponential function was sought which would describe the observed changing characteristics of the cadmium sulfide. The boundary conditions determined from tests specified that the function must have a value of 1 at launch and reach a maximum value of $[1 + K(max)]$. The cumulative aspect of the desorption process implied an integral process which was normalized relative to the observed illumination. These considerations led to postulation of the following expressions to describe the aging phenomena.

$$dR[E(z, t), t] = K(E, t, z)\, dR \qquad (4)$$

where

$dR[E(z, t), t]$ = the resistance of a detector of width dz and length ℓ, illuminated at intensity E(dz, t) which is a function of time t

$K(E, t, z)$ = aging effect on the detector segment dz

$$K(E, t, z) = \left\{ 1.0 + K(\max) \left[\frac{\int_0^t \exp\left(\frac{-E(t, z)t}{CN\ E_0}\right) dt}{\int_0^\infty \exp\left(\frac{-E(t, z)t}{CN \cdot E_0}\right) dt} \right] \right\} \quad (5)$$

where

$K(\max)$ = the maximum value of aging gain determined as a function of the initial and final detector resistance values determined from tests

$$= \frac{R_F}{R_I} - 1$$

R_F = the final resistance value determined from aging tests

R_I = the initial resistance value determined from aging tests

$E(t, z)$ = the time history of illumination (in lm/m^2) observed at coordinate z

E_0 = a reference illumination selected as Earth's illuminance or 135,576 lm/m^2 (12,600 ft-cd)

CN = the aging time constant of a fully exposed detector at the reference illumination (determined empirically to be 15 from the results of a 90-day aging test)

The results of the aging test and the model development will be discussed more fully in the section describing the cruise Sun sensor life test simulation results.

In general, the resistance of the CdS detector is a function of temperature as well as illumination. Extensive testing of the CdS detectors, however, has revealed an unpredictable resistance change of less than 1% in the temperature range of interest (15.5 to 48.8°C). For this reason, temperature effects are not included in the mathematical model of the CdS detector.

In summary, the resistance of a nonuniformly illuminated, aging CdS detector is the sum of the partial resistance of the segments of that detector and can be expressed as follows:

$$R[E(z, t), t] = \int_{-w/2}^{w/2} dR[E(z, t), t]$$

$$= \int_{-w/2}^{w/2} \frac{K(E, t, z)\, RU[E(z)]}{w}\, dz$$

where

$R[E(z, t), t]$ = the resistance of a nonuniformly illuminated detector with aging

III. THE MARINER 1971 CRUISE SUN SENSOR

A. Physical Description

The physical configuration of the Mariner 71 cruise Sun sensor is illustrated in Fig. 4. All four of the cruise cadmium sulfide photoconductors are fitted in glass-filled teflon bushings and mounted on a single aluminum base. Precision-machined shadow bars are bolted to the aluminum base over each detector such that one-half width of the cadmium sulfide photodetectors is shadowed and one-half width is fully illuminated if a point source of light is aligned with the cruise sensor null axis.

Figure 5 is a simplified illustration of the field of view of a single cruise sensor. The error measurement field of view measures ±2.25 deg off the null axis in the error measurement plane. (The error measurement plane contains the null axis and is perpendicular to a vector in the surface of the photodetector which is parallel to the shadow line produced by the shadow bar along the length of the detector.) The off-axis field of view measures ±20 deg off the null axis in a plane perpendicular to the error measurement plane.

The location of the cruise Sun sensor assembly on the Mariner 71 spacecraft was selected to minimize straylight interference and the primary field-of-view obstructions. The cruise sensor was mounted on the outrigger at Bay III, between the octagon structure and the solar panels with the nominal pitch and yaw null axis aligned with the Sun line (Fig. 6).

B. The Theory and Operation of the Mariner 1971 Cruise Sun Sensor

The Mariner 71 cruise Sun sensor is designed to measure the angular offset between the sun line[1] and the null axis of the cruise sensor when the angular error is measured in the error measurement plane for that axis (Fig. 5).

Figure 7 illustrates the principle of cruise sensor operation for a point source of light at an infinite distance from the detector. When the light source is aligned with the null axis of the sensor unit, equal portions of each detector are illuminated and shadowed. In this configuration the resistance of each detector is ideally equal and the error voltage is zero. As the light source is moved off the null axis, the illuminated area of one detector increases, reducing its resistance, and the illuminated area of the other detector decreases, increasing its resistance. The net change in resistance is observed as an error voltage as follows:

$$V_{error} = V_r \frac{(R_1 - R_2)}{\left(R_2 + R_1 + \frac{R_1 R_2}{R_L}\right)} \tag{6}$$

[1] The negative roll axis is the nominal cruise Sun sensor null axis.

where

V_r = a constant reference voltage

R_1 = resistance of detector 1

R_2 = resistance of detector 2

R_L = the equivalent load resistance

In the angular region where the increase in resistance of one detector equals the decrease in resistance of the other detector such that $R_1 = R - \Delta R$, $R_2 = R + \Delta R$, and $R_L \gg R$, the cruise Sun sensor characteristic is approximately linear. In this situation Eq. (6) has the following form:

$$V_{error} = -\frac{V_r \Delta R}{R} = \left(\frac{-V_r C}{R}\right)\phi \qquad (7)$$

where

R = detector null axis resistance

$\Delta R = C\phi$ = change in resistance due to the angular position error ϕ

C = a function of the detector material, shadow bar arrangement, null axis resistance, and the aging characteristic of the detector material.

Assuming all other factors are equal, C will be the same for each detector if and only if each detector has equal aging characteristics.

Graphically the proof may be presented as in Fig. 8. Figure 8(a) shows a single axis detector pair and their shadow bar arrangement. Figures 8(b) and (c) illustrate the aging gain and the resistance per unit width respectively over the detector widths prior to aging. Note that the total resistance of each detector (the area under each resistance per unit width curve) is equal at this time.

After a suitable period of exposure to a point source of light, the aging gain and resistance per unit width of each detector are illustrated in Figs. 8(d) and 8(e), respectively. The aging of the exposed portion of detector 1 has exceeded that of detector 2, resulting in a larger total resistance for detector 1.

There are two operational effects of this unequal distribution of resistance over the detector width of a sensor pair:

(1) The null axis of the detector has now moved to a new position, illustrated in Fig. 8(f). In this position the total resistance of each detector (area under the resistance per unit width curve) is equal, as illustrated in Fig. 8(g).

(2) The change in resistance per unit of angular error C for each detector in this example is different. This difference is manifested as a change in the Sun sensor scale factor.

The above case illustrates how small unbalances in the idealized detector characteristics can cause substantial cruise sensor null offsets. The next section describes the mathematical model of the cruise Sun sensor used in the attempt to duplicate the observed Mariner 71 Sun sensor performance.

C. The Mariner 1971 Cruise Sun Sensor Model

The method of determining a detector's resistance as a function of varying illumination and aging has already been defined in Eq. (4). Once the resistance of a cruise sensor detector pair is known, Eq. (6)[2] defines the error signal to the attitude control electronics and flight telemetry systems. Therefore, a complete description of cruise sensor operation will result when the illumination level over the detector width is determined such that the observed pitch and yaw flight performance and ground-test performance are duplicated.

Accurate determination of the illumination profile over the detector width is the single most important step in reproducing the observed Sun sensor performance. The solar radiation reaching each point on the detector's surface is a function of the following factors:

(1) The light source intensity.

(2) The angular diameter of the light source observed at the sensor.

(3) The orientation of the sensor null axis relative to the Sun line.

---

[2] Equation (6) defines the error signal during normal operation only. Abnormal operation is discussed subsequently.

(4) The reflected light from the surfaces within the cruise sensor housing.

(5) The sensor shadow bar arrangement.

The mathematical model for the illuminance at each point on the detector surface including the above factors is developed below.

The illuminance of a spherical light source is a function of the radial distance from that source, and may be expressed as follows:

$$I(D_1) \times D_1^2 = I(D_2) \times D_2^2 \tag{8}$$

where

$I(D_1)$ = observed illuminance at radial distance D_1 from a light source

$I(D_2)$ = illuminance at a radial distance D_2 from the same light source as observation $I(D_1)$

The angular diameter of a spherical light source can be evaluated from Eq. (8) if the radius of the source is constant. This says that

$$\frac{r}{D_1} = \sin(\theta_1) \tag{9}$$

where

r = the constant radius of a spherical light source

D_1 = the radial distance from the center of the light source to the observer

$2\theta_1$ = the angular diameter of the light source of radius r at a distance D_1 from the observer.

Substituting Eq. (9) into Eq. (8) reveals:

$$\frac{I(D_1)}{\sin^2(\theta_1)} = \frac{I(D_2)}{\sin^2(\theta_2)} \tag{10}$$

Figure 9 is a cutaway view of a Mariner 9 cruise Sun sensor. Illustrated are the angular diameter of the light source (2θ), the sensor null axis pointing error (ϕ), and the height of the shadow bar above the detector surface (h). The illuminance is evaluated as a function of z, where z is the linear measure of the distance from the center of the detector.

$$E(z) = E(D)\, A(z)\, \left|\cos(\gamma)\right| + RL[1.0 - A(z)] \qquad (11)$$

for $z_F \leq z \leq z_Z$

$$E(z) = E(D) \qquad (11a)$$

for $-0.025 \text{ in} \leq z < z_F$

$$E(z) = RL \qquad (11b)$$

for $z_Z < z \leq 0.025 \text{ in}$

where

z_F = that point on the detector surface where all of the solar disk can first be observed = $-h \tan(\theta - \phi)$

z_Z = that point on the detector surface where the solar disk first completely disappears = $+h \tan(\theta + \phi)$

E(D) = the maximum illumination observed at distance D from the light source

E(z) = the illumination at detector width coordinate z

γ = the angle of incidence of the light rays on the detector surface = $\tan^{-1}(z/h)$ for $z_F \leq z \leq z_Z$

h = the height of the shadow bar above the detector surface = 1.61 cm (0.633 in.)

A(z) = that fraction of the light source disk observed at coordinate z for $z_F \leq z \leq z_Z$.

The expression for A(z) is derived in Appendix A and is expressed as follows:

$$A(z) = 0.5 + \frac{\left[X(z)\sqrt{S^2 - X(z)^2} + S^2 \sin^{-1}\left(\frac{X(z)}{S}\right)\right]}{\pi S^2} \tag{12}$$

where

$X(z) = D \cos^2\theta \tan\left[\phi - \tan^{-1}(z/h)\right]$

$S = r \cos\theta$

θ = the angular radius of the Sun

ϕ = the error angle measured from the null axis

It can be demonstrated that the portion of the cadmium sulfide detector which observes no part of the solar disk is illuminated at a low intensity. Simulation results and Sun sensor tests indicate that the light intensity in the shadowed detector region is about uniform and is a function of the ambient illumination level and the angular diameter of the light source, assuming the Sun is within 0.5 deg of the null axis. The reflected light function was selected such that the flight observed rate of change of the spacecraft deadband width was closely approximated by the flight simulation. The proportionality constant was determined by selecting the light intensity in the shadowed portion of the detector so that the evaluated value of the detector null resistance agreed with the known resistance value at Earth.

$$RL = (1185 \pm 100)\, E(R)\theta^2 \tag{13}$$

In summary, Eq. (11) gives an expression for the illumination at any point on the detector width, assuming that the illumination is uniform along the detector length. When this result is substituted into Eq. (4), the resistance of a detector, including aging, can be evaluated if the illumination history is known.

All the analytic tools have been presented which fully describe the Mariner 71 cruise sensor operation. However, discussion of the Sun sensor simulation will be delayed until models for the acquisition Sun sensors and

the control electronics are developed so that the Sun sensor operational discussion can include observed flight performance.

IV. THE MARINER 1971 ACQUISITION SUN SENSORS

A. Physical Configuration

The acquisition sensors consist of four units, each with three detectors mounted as shown in Fig. 10. The acquisition detectors are secured to the gas jet manifold assemblies on the ends of the solar panels to obtain a potentially unobstructed 4π steradian acquisition field of view.

Figure 11 shows a pair of acquisition sensors and illustrates the field stop and shadow bar arrangement.

The field stop ensures that forward-looking acquisition detectors do not observe the Sun during normal cruise operation. The shadow bar arrangement of the rear-looking acquisition detectors prevents the detectors of each axis from having an excessive overlapping field of view.

The three-dimensional field of view of an acquisition detector can be displayed in two dimensions using the spacecraft clock and cone angles. Figure 12 illustrates the field of view of the pitch axis acquisition sensors; Fig. 13 illustrates the field of view of the yaw axis acquisition sensors. Note that each set of acquisition sensors from each axis has an approximate 4π steradian field of view, which ensures that the Sun will produce an error signal in both axes if the cone angle of the Sun line exceeds 5-3/4 deg.

B. Acquisition Sun Sensor Performance Model

The cadmium sulfide light-sensitive detectors used in the acquisition detectors are identical to the ones used in the cruise Sun sensors. The resistance of a fully illuminated acquisition detector can be determined from Eq. (1) if the illuminance is known. The illuminance from the Sun observed by an acquisition detector can be evaluated from Eq. (11) if the following additional considerations are made:

(1) The Sun has a very small angular diameter relative to an acquisition sensor's field of view. Therefore, the following analysis will assume that the full solar disk is always observed by an acquisition detector; i.e., $A(z) = 1$ in Eq. (4).

(2) The angle of incidence (γ) of the Sun's light rays on the acquisition detector face is measured between the vector perpendicular to the detector face and the vector to the Sun.

Figure 14 illustrates the results of a test where the resistance of an acquisition detector was determined as a function of the angle between the vector perpendicular to the detector surface and the nominal pointing direction of a 64,560-lm/m^2 (6,000-ft-cd) light source. Actual test data and the theoretical resistances evaluated using Eq. (11) and Eq. (3) are in good agreement for angles less than 30 deg. After 30 deg some of the radiant energy is reflected from the detector surface, which results in a more rapid resistance increase than theoretically predicted. A similar test revealed that the field stop on the four acquisition detectors looking toward the Sun produces a resistance character illustrated in Fig. 15. Since the introduction of a shadow bar requires that the angular diameter of the light source be considered in addition to the complexities of reflected and stray light, the acquisition sensor model selected used the resistance characteristics illustrated in Figs. 14 and 15, and these resistance values were shifted up and down as a function of the light intensity value at a zero pointing error. For example, the resistance of a side-looking detector illuminated by a 32,280-lm/m^2 (3,000-ft-cd) source at 60 deg from the normal to the detector surface would be determined as follows:

(1) Determine the basic detector resistance for a 60-deg angle and 64,560-lm/m^2 (6,000-ft-cd) source from Fig. 14.

(2) Subtract the resistance value of the detector at a zero degree angle and 64,560-lm/m^2 (6,000-ft-cd) illumination.

(3) Add the resistance value determined from Eq. (11) and (3) for the illumination desired (32,280 lm/m^2, 3,000 ft-cd).

At this time there is no accurate method of verifying the above method of acquisition detector resistance evaluation. However, this model verified the observed Mars orbital Sun sensor "out of regulation," periods which were entirely a function of the resistance of the acquisition sensors. A discussion of the acquisition sensor simulation results will be given in Section VI.

V. THE MARINER 1971 PITCH AND YAW AXIS CONTROL ELECTRONICS

A. Introductory Remarks

The Mariner 9 pitch and yaw axis attitude control electronics circuit is shown in Fig. 16. The Sun sensor bridge contains 12 acquisition and 4 cruise variable resistance light detectors and a ±12.4-V zener diode voltage-regulated power supply.

After the spacecraft was launched it was discovered that the voltage drop across the Sun sensor bridge was not large enough to cause the zener diodes to conduct current and regulate the voltage across the Sun sensor bridge. As a result of the unregulated voltage across the Sun sensor bridge, all perturbations in the ±26-V power supply were observed as perturbations in the error signals at the switching amplifiers which control the attitude control gas jets. When the Sun sensors produced an error signal which caused the gas jets to be fired, the current drain through the gas valves loaded down one polarity of the 26-V supply such that the gas jets were held on until the derived rate network was charged up sufficiently to reduce the error voltage below the switching amplifier threshold.

Laboratory tests revealed that the pitch and yaw axes gas jets would remain on for about 75 ms, and this condition would exist until the Sun sensor bridge resistance increased sufficiently to allow the zener diodes to begin to regulate the sensor supply voltage. The pitch and yaw axis rate increments imparted to the spacecraft due to the gas jets firings could be evaluated from the position telemetry error signals as illustrated in Fig. 17.

The rate increment is determined from Fig. 17 as follows:

$$\omega_1 = \frac{\Delta\theta}{t_1} + \frac{\Delta\theta}{t_2} \tag{14}$$

where

ω_1 = the gas jet rate increment, a known value

$\Delta\theta$ = the spacecraft position deadband width, an unknown value because the voltage across the sensor bridge was not known

t_1, t_2 = the time between gas jet firings

As the resistance of the Sun sensor bridge increased, the cruise sensor scale factor increased so that the spacecraft position deadband decreased. If the rate increments imparted to the spacecraft due to the gas jet firings is assumed constant during this time, the ratio of deadband widths can be determined (Ref. 3) as follows:

$$\omega_2 = \frac{\Delta\theta_2}{t_3} + \frac{\Delta\theta_2}{t_4} \tag{15}$$

Equating the rate increments in Eqs. (15) and (16) we find that

$$\frac{\Delta\theta_2}{\Delta\theta_1} = \frac{t_3 t_4 (t_1 + t_2)}{t_1 t_2 (t_3 + t_4)} \tag{16}$$

If the deadband width at some time is known, or if the gas jet rate increments are known accurately, the deadband width can be determined as a function of time. Figure 18 shows the pitch and yaw axis deadband widths evaluated from flight telemetry data. Two methods are used in the evaluation, one assumed a known deadband width at launch, and the other assumed a known gas jet rate increment. Both methods show deadband values which agree closely during the entire out-of-regulation period (Ref. 3).

The deadband widths are functions of the voltage across the Sun sensor bridge, which in turn is a function of the resistance of each light detector. With the Sun sensor models developed in the previous pages, the resistance history of each detector can be calculated, but to determine the deadband width history which corresponds to the resistance history requires that an analytic model of the pitch and yaw axis control circuit be developed.

B. Attitude Control Electronics Model

Figure 19 is an analytic model of the pitch and yaw axis control circuit. Illustrated are the power supply voltage levels, the variable resistance cruise detectors, the equivalent resistance of the acquisition detectors, and

the equivalent load resistance on each cruise detector circuit. The circuit loop equations are as follows:

$$\begin{array}{rcl} V_1 & = & \left| \begin{array}{ccccc} (R_1 + R_P + R_L) & -R_L & R_P & R_P & 0 \\ -R_L & (R_2 + R_P + R_L) & R_P & 0 & R_P \\ R_P & R_P & (R_3 + 2R_P) & R_P & R_P \\ R_P & 0 & R_P & (R_4 + R_P + R_L) & -R_L \\ 0 & R_P & R_P & -R_L & (R_5 + R_P + R_L) \end{array} \right| \left| \begin{array}{c} I_1 \\ I_2 \\ I_3 \\ I_4 \\ I_5 \end{array} \right| \\ V_1 & = & \\ 2\,V_1 & = & \\ V_1 & = & \\ V_1 & = & \end{array} \qquad (17)$$

where

R_1, R_2, R_4, R_5 = variable-resistance cruise sensor light detectors

R_3 = the equivalent resistance of the 12 acquisition detectors

R_L = the equivalent load resistance of the telemetry and switching amplifier = 55.2 kΩ

R_P = the incorrectly sized current limiting resistors = 1.91 kΩ

Analysis of the telemetry and switching amplifier load circuit R_L reveals that the gas jets will fire when the current flow in the equivalent load resistance exceeds 21.6×10^{-6} A. The current flow from one axis is $(I_1 - I_2)$ and may be evaluated by expressing the matrix equation (18) as partial matrices in the following form:

$$\left| \begin{array}{c} \overline{B}_1 \\ \overline{B}_2 \end{array} \right| = \left| \begin{array}{cc} A_{11} & A_{12} \\ A_{21} & A_{22} \end{array} \right| \cdot \left| \begin{array}{c} \overline{X}_1 \\ \overline{X}_2 \end{array} \right|$$

where

$$\overline{X_1} = \left| \begin{array}{c} I_1 \\ I_2 \end{array} \right|, \quad \overline{X_2} = \left| \begin{array}{c} I_3 \\ I_4 \\ I_5 \end{array} \right|, \quad \overline{B_1} = V_1 \left| \begin{array}{c} 1 \\ 1 \end{array} \right|, \quad \overline{B_2} = V_1 \left| \begin{array}{c} 2 \\ 1 \\ 1 \end{array} \right|$$

$$\overline{A_{11}} = \begin{vmatrix} (R_1 + R_P + R_L) & -R_L \\ -R_L & (R_2 + R_P + R_L) \end{vmatrix}$$

$$\overline{A_{12}} = \begin{vmatrix} R_P & R_P & 0 \\ R_P & 0 & R_P \end{vmatrix}$$

$$\overline{A_{21}} = \begin{vmatrix} R_P & R_P \\ R_P & 0 \\ 0 & R_P \end{vmatrix}$$

$$\overline{A_{22}} = \begin{vmatrix} (R_3 + 2R_P) & R_P & R_P \\ R_P & (R_4 + R_L + R_P) & -R_L \\ R_P & -R_L & (R_5 + R_L + R_P) \end{vmatrix} \qquad (18)$$

Solving the set of equations (18) for X_1 we find:

$$\overline{X}_1 = \left[\overline{A_{11}} - \overline{A_{12}}\,\overline{A_{22}^{-1}}\,\overline{A_{21}}\right]^{-1} \left[\overline{B_1} - \overline{A_{12}}\,\overline{A_{22}^{-1}}\,\overline{B_2}\right] \qquad (19)$$

Equation (19) is an expression for I_1 and I_2 in terms of known circuit parameters and Sun sensor resistor elements. Subtracting I_1 from I_2 in Eq. (19) and setting this expression equal to 21.6×10^{-6} reveals that in the unregulated state the deadband in one axis is a function of the position error in the other axis. A computer circuit simulation showed that the maximum cross axis coupling is small (about 2%). In the simulations that follow the cross axis coupling effects will be assumed random and negligible.

At this point, all of the Sun sensor control system element models have been developed. The next section discusses the computer simulations of the Sun sensor elements and compares these results to the existing test and flight data.

VI. THE MARINER 1971 SUN SENSOR LIFE TEST AND SIMULATION RESULTS

A. Introductory Remarks

Construction of a mathematical Sun sensor model is the process of determining a consistent set of mathematical functions which will reproduce the observed Sun sensor performance. Unfortunately, a test facility reproduction of the flight environment is very difficult, so the cruise sensor aging test results could not be exactly reproduced using the computer model.

The principal obstruction in the simulation of the aging test was an accurate reproduction of the light source.

The light source used for the aging tests was a 1-kW zenon short arc lamp. The gap between the lamp electrodes was about 3 mm, with the most intense source of radiation emitted from an area about 1 mm from the smaller electrode. The image of the arc was magnified about 4 times and was projected on an aperture plate. The size of the aperture determined the amount of radiation and the angular diameter the light source used to age the cruise detectors. However, the amount of radiation emitted over the aperture area was not uniform. This can be demonstrated as follows. The measured illumination from a 1.9-cm (0.75-in.) aperture plate is 107,600 lm/m^2 (10,000 ft-cd). If the radiation is uniformly distributed over the aperture area, the measured illumination should be proportional to the aperture area. This relationship can be expressed as follows:

$E = kA$

E = measured illumination

A = area of a uniform light source

$= \frac{\pi d^2}{4}$

d = the aperture diameter

k = a proportionality constant

If the aperture diameter is changed and the radiation is uniform, the measured illumination should obey the following relationship:

$$E_1 = \frac{E_2 A_1}{A_2}$$

$$= \frac{E_2 d_1^2}{d_2^2}$$

During the aging test resistance evaluation sequence, the aperture diameter was reduced from 1.9 cm (0.75 in.) (producing a measured 107,600 lm/m^2 (10,000 ft-cd) illumination) to 0.635 cm (0.25 in.). From the equation above, the measured illumination should have been 11,955 lm/m^2 (1,111.1 ft-cd) if the source radiation was uniformly distributed over the aperture area. The actual measured illumination was 26,900 lm/m^2 (2,500 ft-cd). This evaluation demonstrates that the illumination varies significantly over the aperture area. The cognizant test engineer, L. Schmidt, indicates that the illumination varies by a factor of 4 or more in the vertical direction over the 1.9 cm (0.75-in.) aperture diameter.

As a result of the nonuniform light source, the model development effort was weighted towards duplication of the observed flight performance. Fortunately, a credible model was discovered which closely approximated both the observed flight data and the laboratory life test data. Each test simulation and the flight simulation will be discussed below, and the various components of the sensor models will be discussed when their effects dominate sensor performance.

B. The Cruise Sun Sensor Aging Test (No Rotation)

During this test (Ref. 4) the null axis of a cruise Sun sensor pair was approximately aligned with the rays from a 107,600-lm/m^2 (10,000-ft-cd) light source for 92 days. Twice a week the radiation level was reduced to 26,900 lm/m^2 (2,500 ft-cd) for short periods; the sensors were rotated to balance the detector pair's resistance and the resistance was recorded. Figure 20 shows the resistance of a single detector determined from this test and the resistance determined from a life test simulation.

After the angular diameter and illumination of the light source were determined for various stages in the testing procedure there were two additional steps in determining the cruise Sun sensor model components. The first step was to determine a reflected light level within the detector housing which would produce the observed detector resistance before aging. The reflected light level at the 26,900-lm^2/m^2 (2,500-ft-cd) illuminance was simply determined by a process of trial and error. Since the actual aging took place at an illuminance of 107,600 lm/m^2 (10,000 ft-cd), a relationship between the reflected light levels within the detector housing at different illumination levels was required. Logically, the amount of reflected light within the detector housing should be related to the amount of energy available for reflection, i.e., the angular area and illuminance of the light source. Equation (13) is the expression used in the simulations to determine the reflected light level as a function of the angular radius and the illuminance of the light source. Initially, the proportionality constant in Eq. (13) could not be adjusted so that flight simulations and life test simulations could be reproduced from the same model. Evaluation of the life test setup revealed that light reflections from the test equipment probably introduced some additional light into the shaded portion of the cruise detectors. Simulations indicated this value was probably between 1,614 and 2,152 lm/m^2 (150 and 200 ft-cd). When the additional amount of reflected light was introduced into the life test simulations, the same straylight model produced good life test and flight data correlation. Further comments on the sensitivity of the cruise Sun sensor to the reflected light levels within the detector housing will be delayed until the flight data simulation discussion.

The second step in determining cruise sensor model components was to determine an aging function which would approximately produce the observed rate of resistance increase in the detector. The detector aging model development depended on information obtained during a second part of the aging discussed below.

C. The Cruise Sun Sensor Aging Test (With Rotation)

During this portion of the aging test, the null axis of a cruise Sun sensor pair was aligned with the rays of a 107,600-lm/m^2 (10,000-ft-cd) source for 92 days. Twice a week the sensor was rotated ±30 min of arc and kept in that position for 20 min. Following the rotation sequence the

radiation level was reduced to 26,900 lm/m^2 (2,500 ft-cd), the sensors were rotated to balance the resistance of the detector pair, and the resistance was recorded. Figure 21 shows the detector resistance determined from this test and from a test simulation.

The final steady-state detector resistance value due to aging by a fixed-intensity light source was about double the initial resistance value. The exponential aging model described by Eq. (5) worked well in the simulation models and also provided an explanation for the apparent difference in the results of the two laboratory aging tests.

The aging model described by Eq. (5) states that the rate of aging is always positive as long as the detector is illuminated. Therefore, during the rotation sequences the rate of aging in the normally low intensity regions of the detector is greatly increased while the rate of aging in the normally higher intensity regions of the detector is only slightly reduced. To compensate for this effect the simulation model assumed, for aging purposes, that the average effect of rotation in the life tests and due to normal flight limit cycle motion could be modeled by increasing the level of the reflected light intensity in the shaded region of the detector. Figure 22 illustrates the assumed light intensity profiles over the detector widths for the unrotated life test and for the rotated life test. Also shown in Fig. 22 are the aging gain values at selected times. The aging gains in the fully illuminated regions of each detector in both tests are identical, but the aging gain of the rotated detectors increases much more rapidly in the low illuminance regions than the aging gain of the nonrotated detectors.

The simulated detector resistance values resulting from these aging tests have already been shown to be very close to actual aging test values in Figs. 20 and 21.

Although the simulated aging tests do not identically reproduce both of the observed aging test results, the idealized test environment and test procedures assumed in the computer simulations probably account for most of the differences.

D. Mariner 9 Flight Simulation

The object of this simulation effort was to evaluate mathematical Sun sensor models which attempted to reproduce the observed Sun sensor flight performance data. The flight data that contained information about Sun sensor performance is listed below:

(1) The pitch and yaw axis limit cycle data used to evaluate the deadband values.

(2) The voltage across the sensor bridge was known to be greater than 24.8 but less than 26 V when the start of normal operation was observed.

The constraints imposed on the sensor models used in the simulation were as follows:

(1) The reflected light and the aging models should be consistent with models used in the aging test simulations.

(2) The illumination and angular diameter of the simulated light source should closely approximate the Sun as it was observed in flight.

The flight simulation results were gratifying. Figure 23 illustrates the Mariner 71 deadband halfwidth calculated from the observed flight telemetry data and the simulated flight deadband halfwidth values. The rate of change of the simulated deadband width was a function of the solar illumination, angular diameter of the Sun, the aging characteristics of the detector material, and the straylight level within the cruise sensor housing.

The deadband width at day 150 could be adjusted by minute changes in the amount of reflected light within the detector housing. For example, the upper simulated deadband width in Fig. 23 assumed 2.79% of the ambient light on day 150 was the reflected light level within the shaded portions of the cruise sensor and the lower simulated deadband width assumed 2.33%.

The cruise sensor is extremely sensitive to the reflected light levels within the shaded portion of the cruise sensor housing. This sensitivity is demonstrated in Fig. 24. The upper figures illustrate the illumination distribution over a detector width for a 0.95-deg-angular-diameter light source at 26,900 lm/m^2 (2,500 ft-cd). The reflected light in the shaded

portion of the cruise sensor housing on the left figure is 1,119 lm/m^2 (104 ft-cd); in the right figure it is 2,733 lm/m^2 (254 ft-cd). The resistance per unit width profiles across the detector widths are illustrated directly below the illumination profiles. Integrating the resistance per unit width across the detector widths reveals that the resistance of the fully illuminated portion of each detector is exactly the same, 681 Ω. The resistance in the fully shaded portion of the detector is 4,617 Ω in the region illuminated at 1,119 lm/m^2 (104 ft-cd) and 2,698 Ω in the region illuminated at 2,733 lm/m^2 (254 ft-cd). The total resistance of the detector with the 1,119-lm/m^2 (104-ft-cd) reflected light level is 6,514 Ω and 4,021 Ω for the detector with the 2,733-lm/m^2 (254-ft-cd) reflected light level. The above values illustrate that a reduction in the reflected light illuminance by about 6% of the ambient light level increases the total detector resistance by about 62%.

The Mariner 71 cruise Sun sensor design is extremely sensitive to the reflected light level within the detector housing and as a result is very susceptible to housing design, shadow bar arrangement, internal coating reflectivity, and reflected straylight from external sources.

A process of trial and error determined that the reflected light model described in Eq. (13) worked well in both the flight performance simulations and the life test simulations.

The detector aging model was largely determined from the life tests. The close correlation between the flight simulations and the actual observed flight performance, in addition to the good agreement in the life test simulations, indicates that the principal aging characteristic can be approximated by a modeling technique similar to the one described in Eq. (5).

Further support for the aging model is presented below. Figure 25 illustrates the simulated resistance values for the acquisition sensor bridge, a single cruise detector, and the total resistance of the entire Sun sensor bridge as a function of time for both sensor models. In both cases the largest resistance change occurs in the cruise Sun sensors as a result of detector aging. Since the detector aging model dominates the change in the sensor bridge resistance and the resultant voltage drop across the Sun sensor bridge, the aging model is reinforced by Fig. 26, which illustrates that the simulated voltage drops across the Sun sensor bridge are at the

desired levels to completely span the time interval when the Mariner 71 Sun sensor went back into complete regulation.

It may be concluded that the flight data simulations were a success. However, because of a lack of testing to confirm some of the modeling techniques, it is not possible to conclude that the simulation models are general enough to accurately simulate other flight situations.

E. Mariner 1971 Acquisition Sun Sensor Simulations

The Mariner 71 Sun sensor configuration has the acquisition sensor bridge as a permanent load across the Sun sensor power supply (Fig. 16). Therefore, to accurately determine the total load resistance of the entire Sun sensor circuit requires that the resistance of each acquisition detector be known as accurately as possible.

The acquisition detector models used the existing measured test data as part of the model, but there was no test data to evaluate the simulated acquisition bridge resistance or the acquisition detector resistance characteristics at different illumination levels. For this reason the Sun sensor simulation in the vicinity of the lighted planet was important since it verified that the acquisition sensor model predicted the orbital out-of-regulation periods very accurately and therefore probably adequately modeled the acquisition sensor response during the transit cruise period.

The Sun sensor simulation of the orbital cruise period assumed that the cruise sensors were completely aged and that the acquisition detectors had not aged at all.

Figure 27 illustrates the total resistance of the cruise sensors, the acquisition sensors, and the entire Sun sensor load resistance during the 1-hour period near periapsis. The zener diodes go out of regulation when the total Sun sensor resistance falls to about 3.1 to 3.2 kΩ. Since the cruise detectors are completely aged their mean resistance is constant, but the acquisition bridge resistance shows an extreme drop in resistance for a short period, reducing the total Sun sensor bridge resistance level below the zener regulation level.

The reason for the sudden acquisition sensor resistance drop is illustrated in Fig. 28. The illuminated portion of the planet is plotted in

spacecraft clock and cone coordinates on 10-min intervals for December 10, 1971, beginning at 12:40.

Figure 27 reveals that from about 12:42 to about 13:35 the Sun sensors were out of regulation. This time interval agrees closely with the observed flight out-of-regulation period.

In Fig. 28 the out-of-regulation time interval is implied within curves B, C, D, E, and F. It is observed that when the lighted portion of the planet illuminated acquisition sensors of both polarities, a low impedance path was created across the acquisition sensor bridge if the light intensity was great enough.

The principal modeling problem in the orbital period simulations was to determine what the lighted portion of the planet looked like to the spacecraft. Reference 5 contained a program listing which determined the position of the planet lighted limb and terminator in spacecraft clock and cone angles. This program was incorporated into the Sun sensor simulation model along with a weighting function to determine how much light was contributed from selected points on the lighted portion of the planet. It was determined that each point on the lighted edge of the planet contributed a percentage of the total planet light proportional to the absolute value of the cone angle of the vector to that point.

Other more complex methods of determining the illumination distributions over the lighted portion of the planet were rejected because of the model development time required. However, future acquisition sensor modeling efforts should include an improved planet illumination distribution model.

VII. CONCLUSION AND RECOMMENDATIONS

The computer simulations described in this report demonstrate that flight performance can be predicted accurately using a complete Sun sensor computer model.

The applicable specification (The Detailed Specification for Acquisition and Cruise Sun Sensors – The Attitude Control Subsystem – Mariner '71 Flight Equipment, ES 50Y993) gives the Sun sensor null offset and scale factor requirements, but does not follow up with a realistic test program

which can give reasonable guarantees that these requirements will be met. The apparent omission in all the specifications is the flight conditions or analysis efforts. The Mariner '71 Sun sensor preflight evaluation testing program was a series of static environment tests which did not reveal potential problems which could result from a variety of flight conditions.

In an attempt to anticipate future Sun sensor environmental and/or operational hazards, the following general plan is proposed:

(1) Determine as accurately as possible the operational characteristic of the light detector material to be used in flight.

(2) Determine the response of the light detector in the various sensor housings and for a variety of environmental conditions.

(3) Construct a mathematical sensor model which will closely duplicate the test results described above.

(4) Integrate the sensor models into a dynamic model of the spacecraft and the attitude control subsystem electronics.

(5) Evaluate the Sun sensor flight performance for all proposed mission operational modes, using the sensor models.

(6) Selectively check model predictions with additional tests.

The above test and evaluation procedure will also establish a Sun sensor performance standard. If the observed test or flight performance deviates from the model predictions, the source of the discrepancy should be resolved.

REFERENCES

1. Clairex Photoconductive Cell Design Manual, Clairex Corp., New York, N.Y., 1966.

2. Stirn, R.J., "Stability of Sintered Cadmium Sulphide Photoconductive Layers," Jet Propulsion Laboratory, Pasadena, Calif., Mar. 27, 1969 (an internal document).

3. Edmunds, R.S., "Recovery of Mariner 9 from Its Anomalous Operating Mode," EM 344-361, Jet Propulsion Laboratory, Pasadena, Calif., 1971 (an internal document).

4. Schmidt, L., "Mariner '71 Sun Sensor Life Test," IOM 343-8-72-102, Jet Propulsion Laboratory, Pasadena, Calif., Feb. 2, 1972 (an internal document).

5. Fleischer, G.E., "Viking '73 Sun Occultation Sensor Field of View Location, EM 344-237 GEF, Jet Propulsion Laboratory, Pasadena, Calif., Aug. 6, 1969 (an internal document).

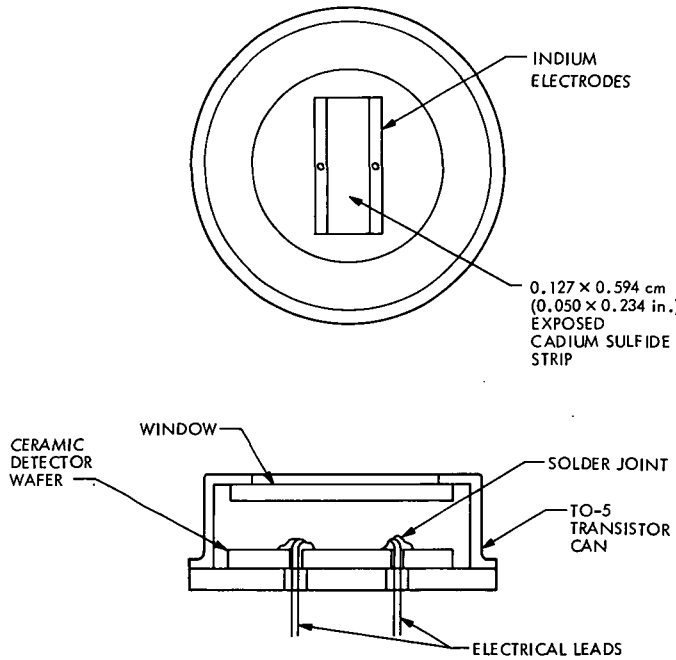

Fig. 1. Cadmium sulfide detector configuration

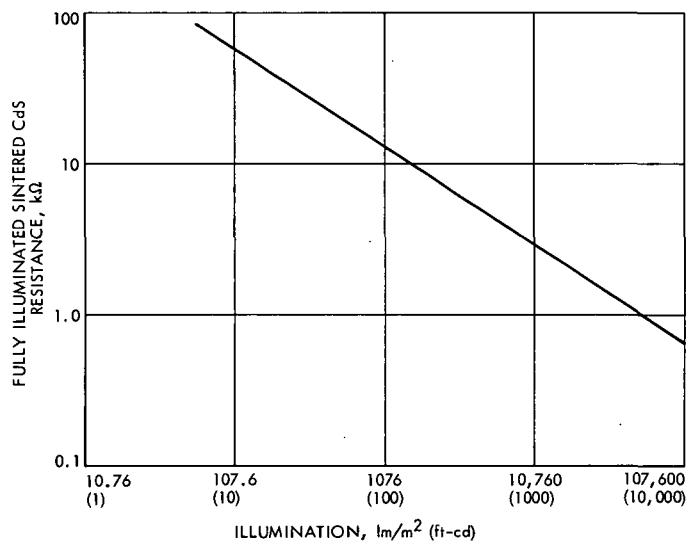

Fig. 2. Fully illuminated CdS detector resistance as a function of illumination

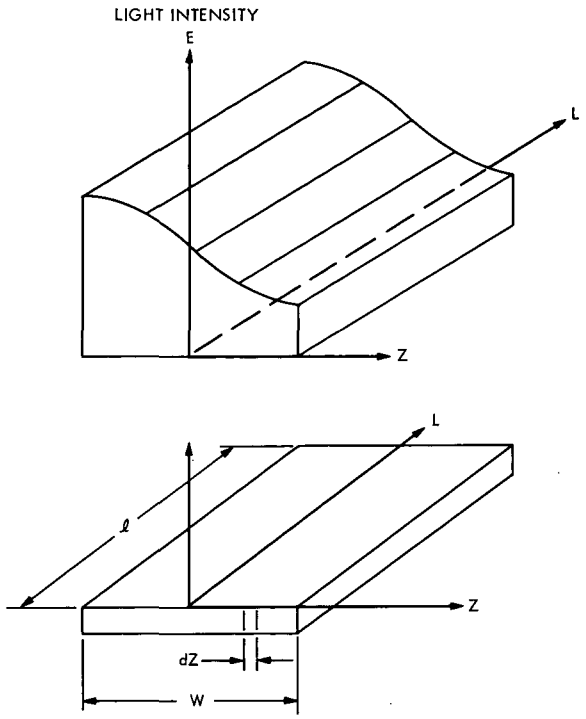

Fig. 3. Detector coordinate system

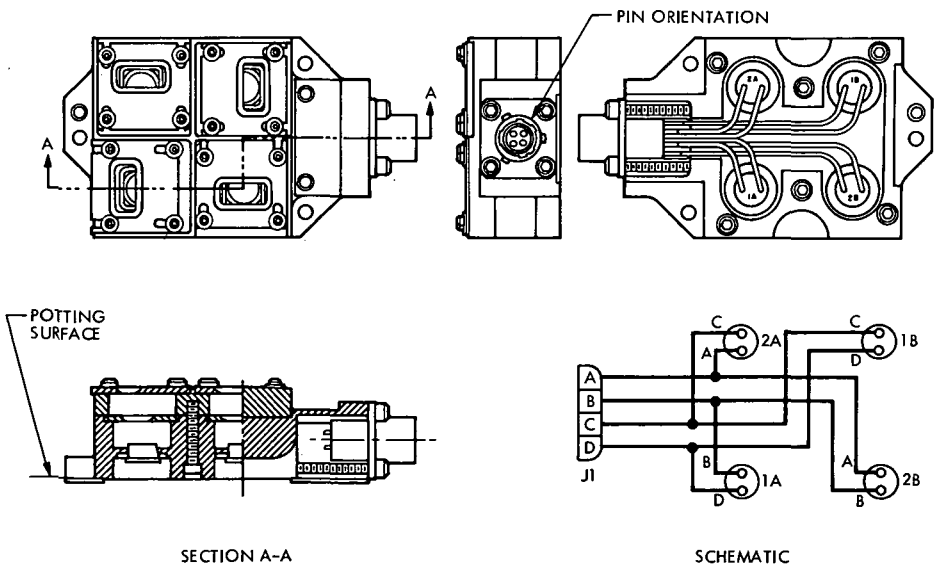

Fig. 4. Mariner 71 cruise Sun sensor configuration

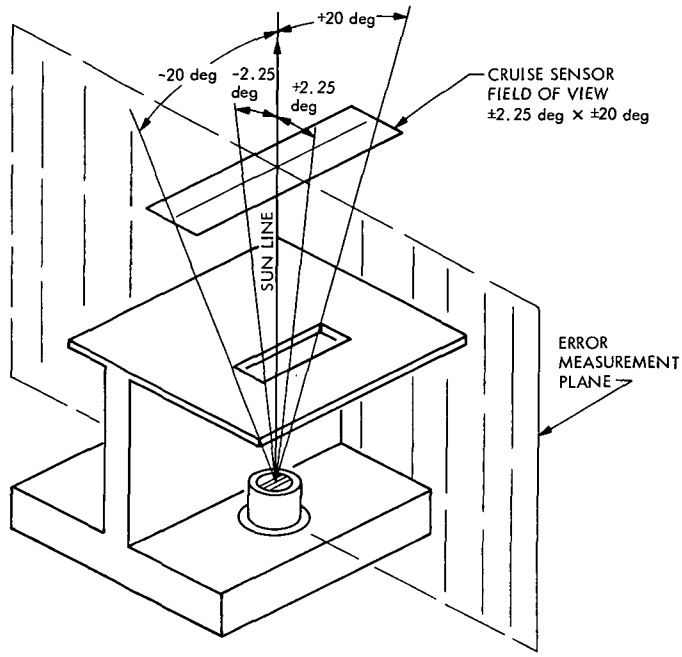

Fig. 5. Mariner 71 cruise sensor field-of-view

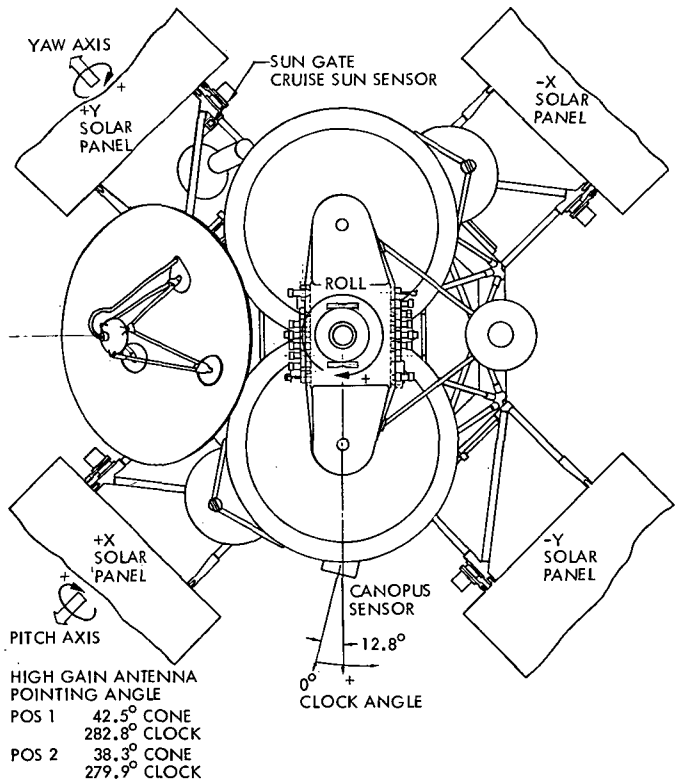

Fig. 6. Sun side (top) view of Mariner 71 spacecraft

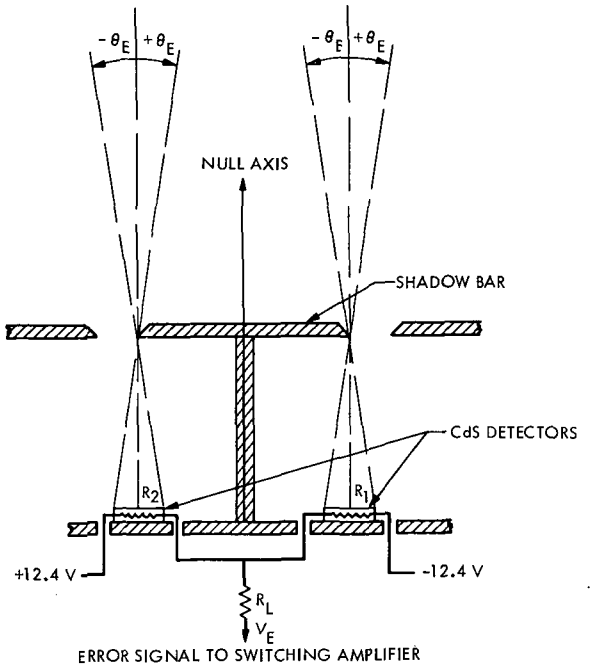

$$V_E = \frac{12.4\,(R_1 - R_2)}{(R_1 + R_2) + R_1 R_2 / R_L}$$

Fig. 7. Theory of cruise sensor operation

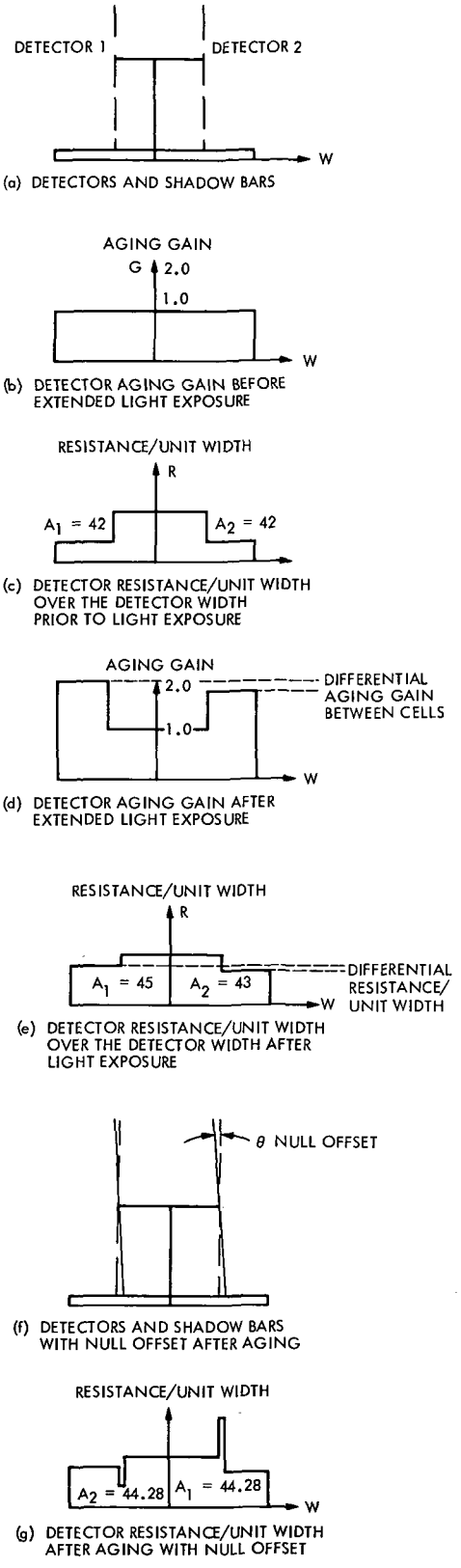

Fig. 8. Idealized detector pair aging with unequal rate of aging

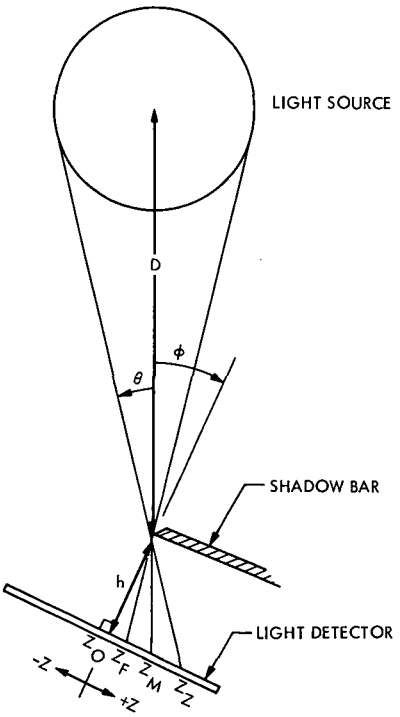

FULL ILLUMINATION PT. = $Z_F = -h \tan(\theta - \phi)$
HALF ILLUMINATION PT. = $Z_M = h \sin(\phi)$
LOW ILLUMINATION PT. = $Z_Z = h \tan(\theta + \phi)$
ϕ POSITIVE DECREASES SHADOW AREA

Fig. 9. Cruise Sun sensor illumination profile over detector width

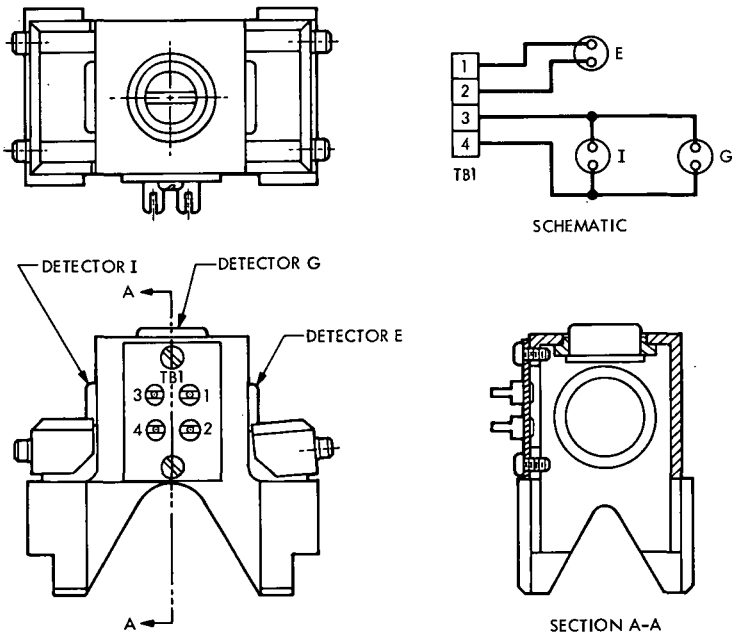

Fig. 10. Acquisition Sun sensor

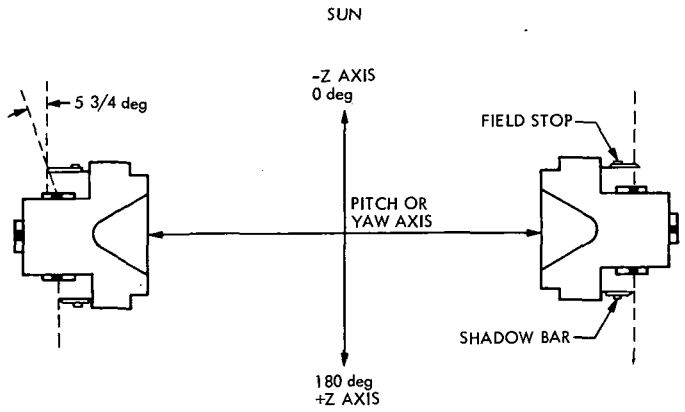

Fig. 11. Acquisition Sun sensor pair showing field stops and shadow bar configuration

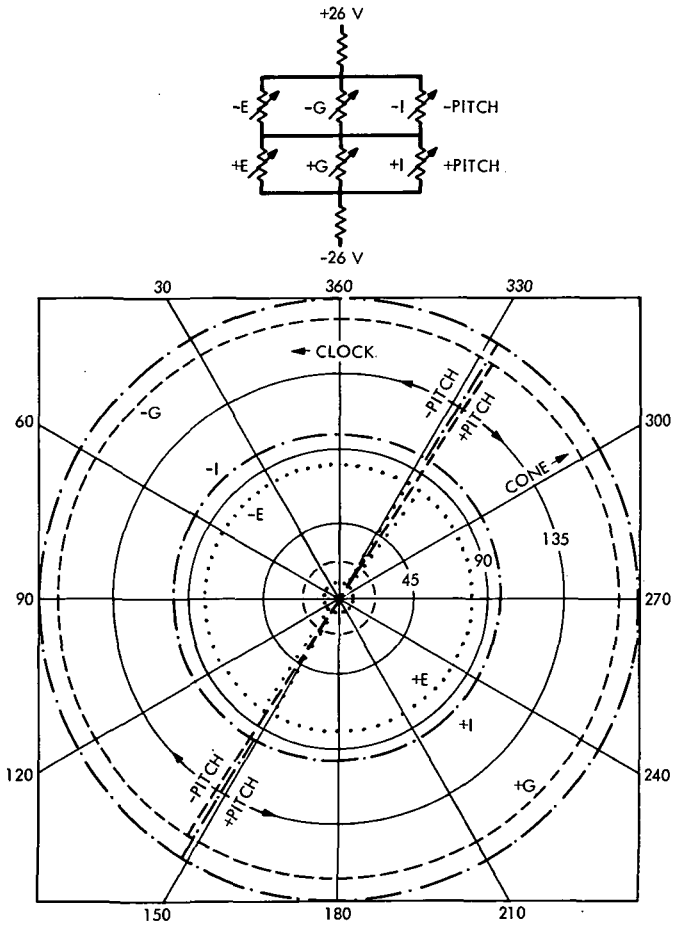

Fig. 12. Mariner 71 pitch axis acquisition Sun sensor field-of-view

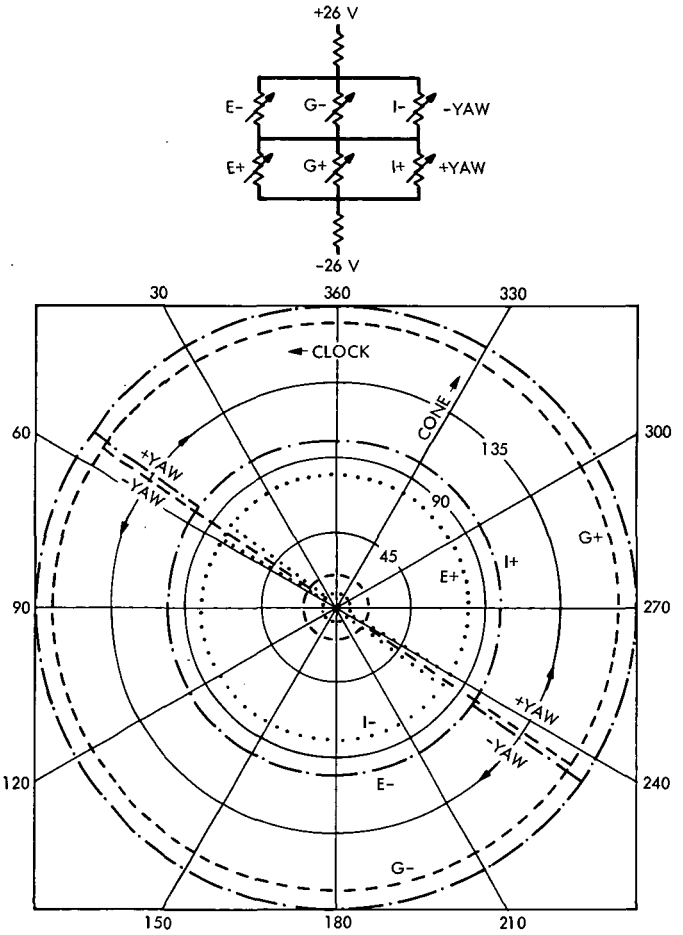

Fig. 13. Mariner 71 yaw axis acquisition Sun sensor field-of-view

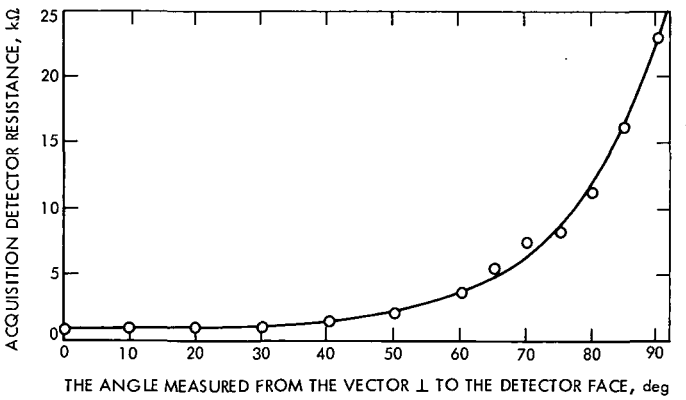

Fig. 14. Acquisition detector resistance vs conical error angle of a 64,560-lm/m^2 (6,000-ft-cd) light source

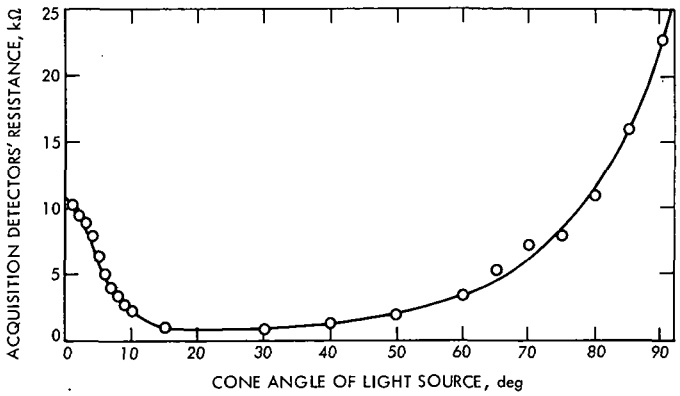

Fig. 15. Forward-looking acquisition detector resistance vs cone angle of a 64,560-lm/m^2 (6,000-ft-cd) light source

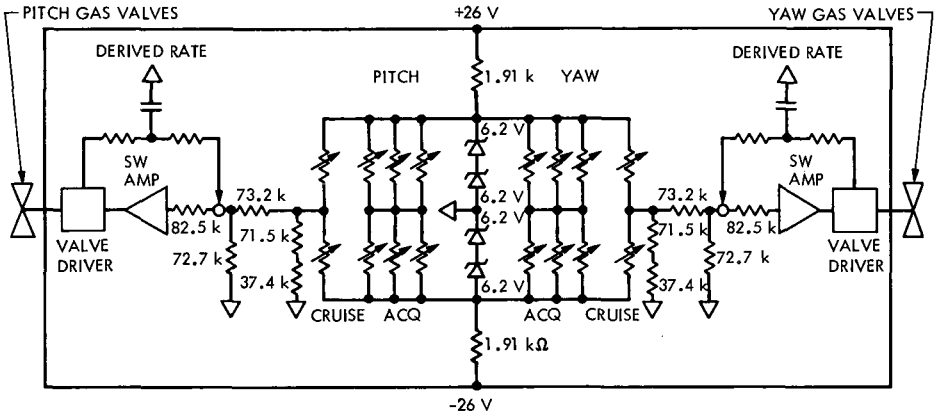

Fig. 16. Mariner 71 pitch and yaw axes Sun sensor control circuit

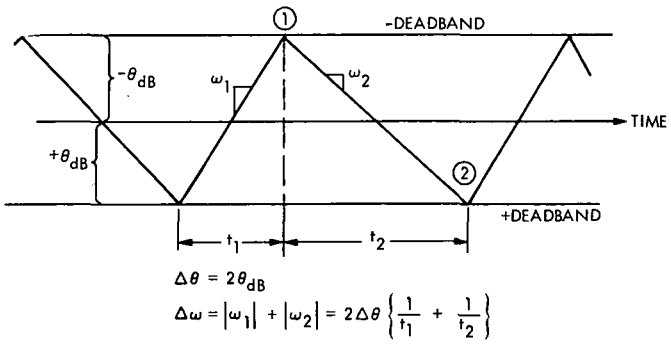

Fig. 17. Evaluation of limit cycle rate increment due to a gas pulse

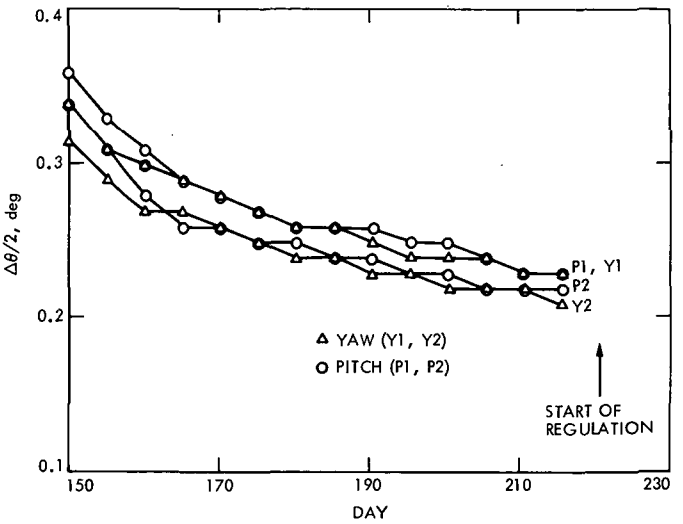

Fig. 18. Estimates of Mariner 9 deadband halfwidth

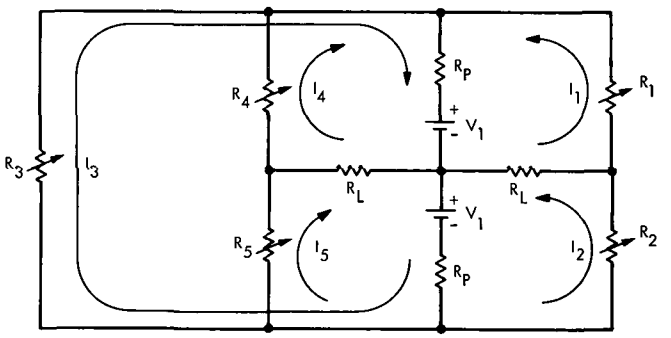

Fig. 19. Analytic pitch and yaw axis control circuit

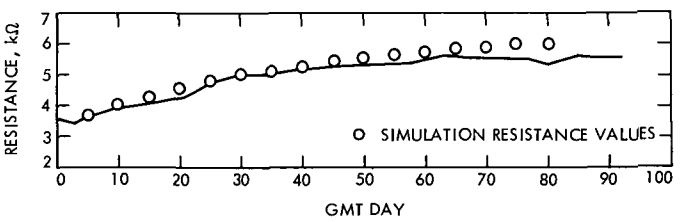

Fig. 20. Mariner 71 cruise detector resistance during a life test without detector rotation

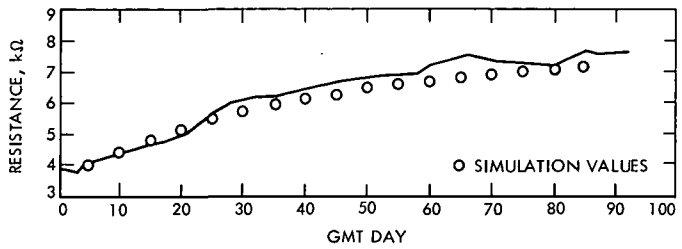

Fig. 21. Mariner 71 cruise detector resistance during a life test with detector rotation

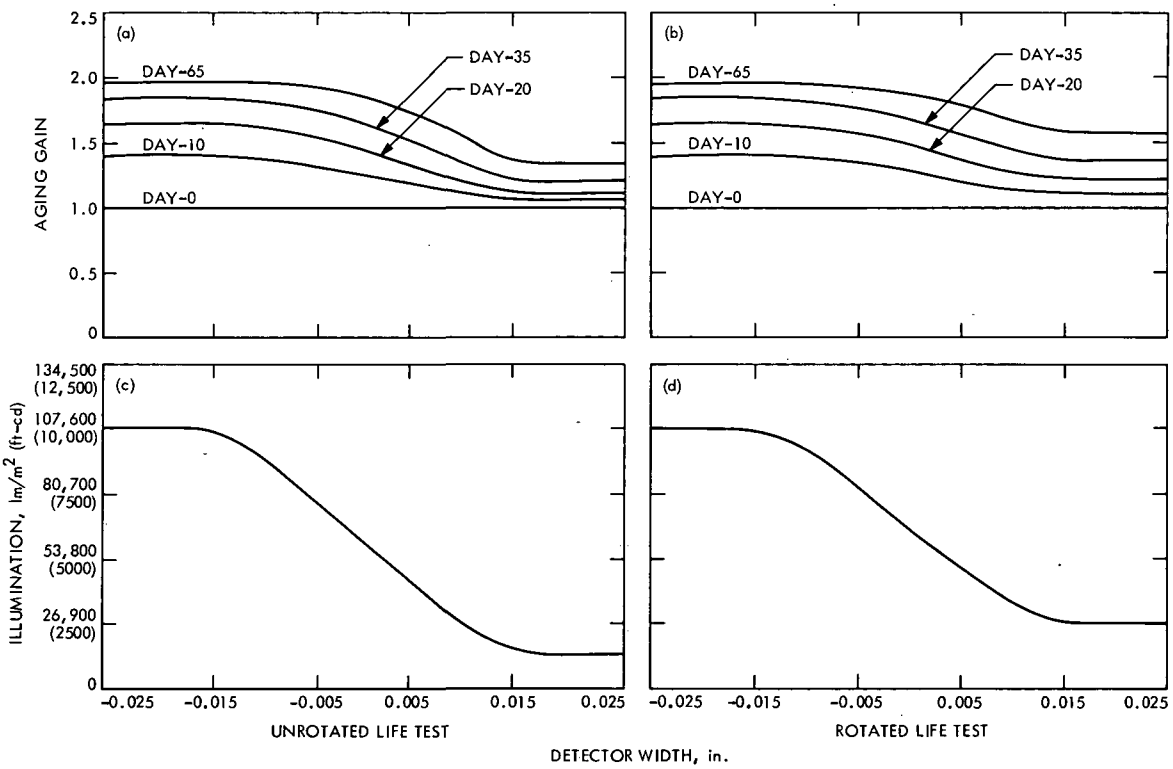

Fig. 22. Aging gain as a function of fixed light intensity and time

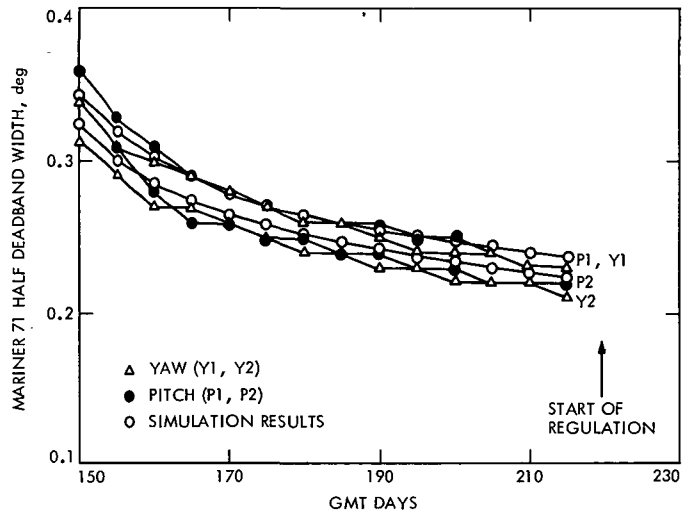

Fig. 23. Comparison of flight-observed half-deadband width to the computer model half-deadband width

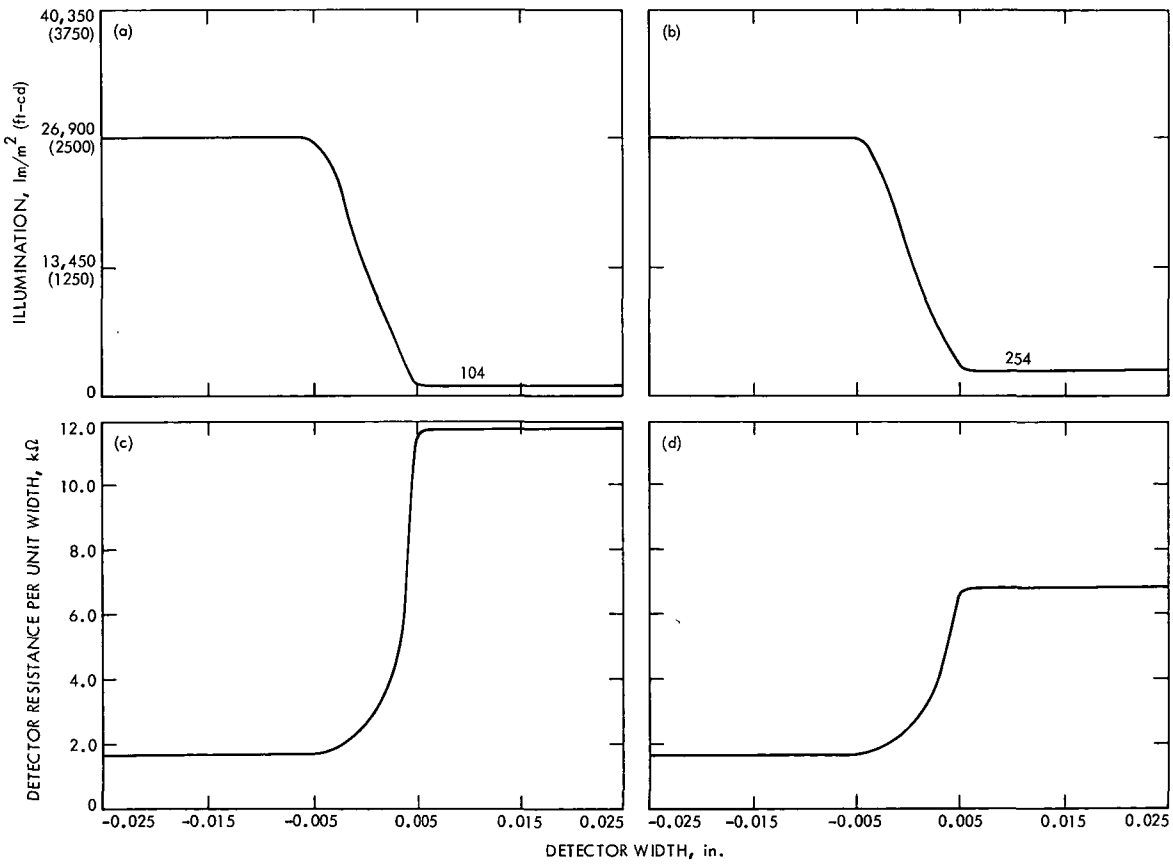

Fig. 24. Cruise sensor sensitivity

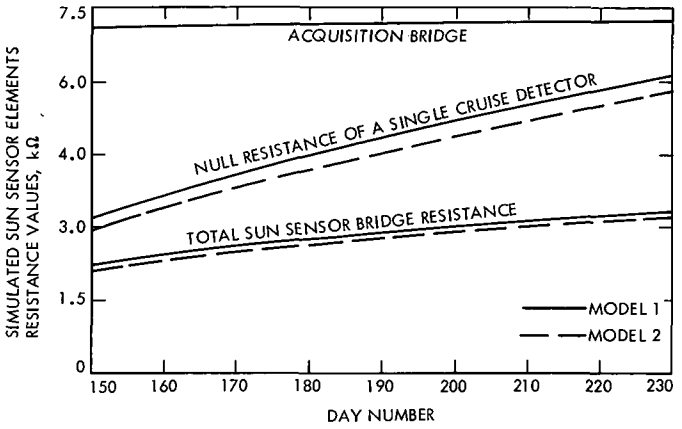

Fig. 25. Resistance values of simulated cruise Sun sensor elements

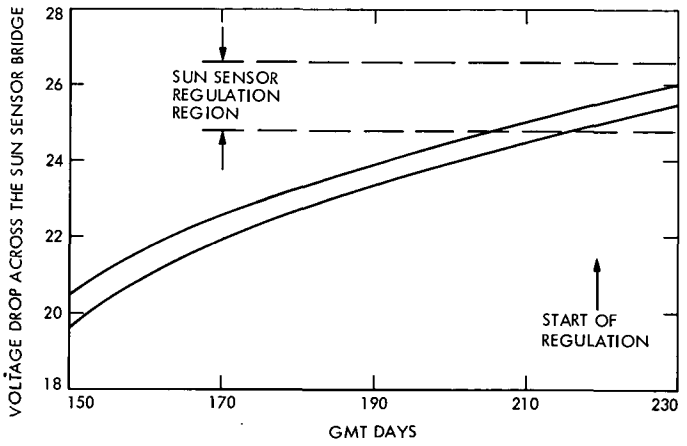

Fig. 26. Voltage drop across Sun sensor bridge

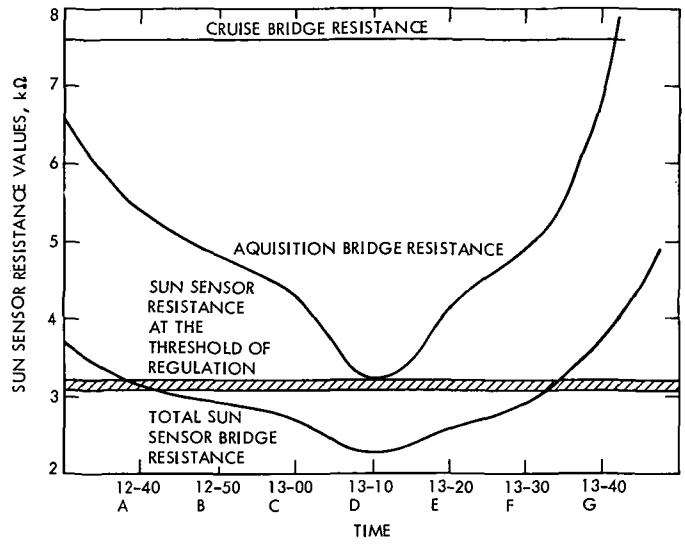

Fig. 27. Sun sensor resistances near periapsis, December 10, 1971

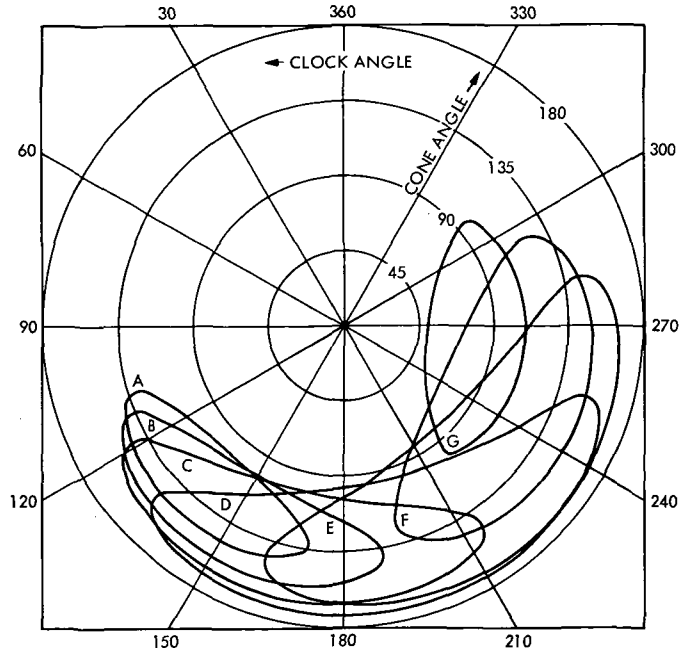

Fig. 28. The illuminated portion of Mars as observed on the spacecraft

APPENDIX

DETERMINATION OF THE ILLUMINATION PROFILE OVER THE CRUISE SUN SENSOR DETECTOR WIDTH

This appendix outlines the derivation of the expression for A(z), the fraction of the light source disk which is observed at coordinate z on the detector width.

Figure A-1 illustrates a uniform-intensity light disk and the relationship to the detector surface. An X-Y coordinate system is established in the plane of the light disk with the origin at the center of the disk. The lighted area is that portion of the plane where

$$X^2 + Y^2 = S^2 \tag{A-1}$$

where $|X| \leq S$, $|Y| \leq S$.

The area of the light disk can be determined as a function of X as follows. An element of area dA illustrated in Fig. A-1 can be expressed as:

$$dA = 2Y\,dX \tag{A-2}$$

Substituting for Y from Eq. (A-1) into Eq. (A-2) and integrating from -S to +X we find:

$$A(X) = 2\int_{-S}^{+X} \sqrt{S^2 - X^2}\, dX \tag{A-3}$$

or

$$A(X) = 0.5 + \frac{X\sqrt{S^2 + X^2} + S^2 \sin^{-1}\left(\frac{X}{S}\right)}{\pi S^2}$$

Figure A-1 also indicates that the X coordinate in the light disk can be related to a z coordinate in the detector coordinate system if the radial distance from the shadow bar to the light disk D_d and the pointing error ϕ are known; i.e.,

$$X(z) = D_d \tan(\phi - \gamma) \tag{A-4}$$

where $\gamma = \tan^{-1}(z/h)$ for $-h \tan(\theta - \phi) \leq z \leq h \tan(\theta + \phi)$.

Substituting Eq. (A-4) into Eq. (A-3) results in an expression for the fraction of the solar disk observed at coordinate z of the detector width.

When θ and ϕ are less than 1 deg, the expression for A(z) may be simplified and expressed as follows:

$$A(z) = 0.5 + \frac{\left[\phi - \frac{z}{h}\right]}{\theta^2}\sqrt{\theta^2 - \left(\phi - \frac{z}{h}\right)^2} + \sin^{-1}\left[\frac{\left(\phi - \frac{z}{h}\right)}{\theta}\right] \Bigg/ \pi$$

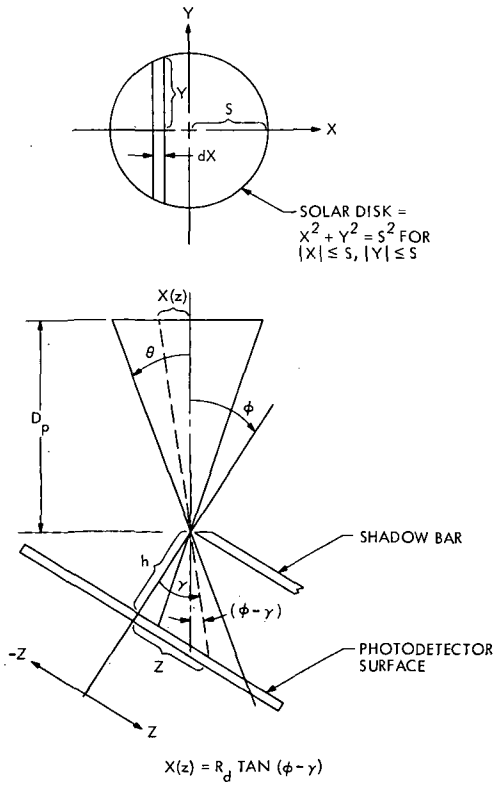

Fig. A-1. Relation of solar disk coordinates to spacecraft detector coordinates

NASA — JPL — Coml., L.A., Calif.